

# Multi-Method Characterization of the High-Entropy Spinel Oxide $\text{Mn}_{0.2}\text{Co}_{0.2}\text{Ni}_{0.2}\text{Cu}_{0.2}\text{Zn}_{0.2}\text{Fe}_2\text{O}_4$ : Entropy Evidence, Microstructure, and Magnetic Properties

Svenja Senkale,<sup>[a]</sup> Marius Kamp,<sup>[b]</sup> Stefan Mangold,<sup>[c]</sup> Sylvio Indris,<sup>[d]</sup> Lorenz Kienle,<sup>[b]</sup> Reinhard K. Kremer,<sup>[e]</sup> and Wolfgang Bensch<sup>\*[a]</sup>

The novel spinel  $\text{Cu}_{0.2}\text{Co}_{0.2}\text{Mn}_{0.2}\text{Ni}_{0.2}\text{Zn}_{0.2}\text{Fe}_2\text{O}_4$  comprising six transition metal cations was successfully prepared by a solution-combustion method followed by distinct thermal treatments. The entropic stabilization of this hexa-metallic material is demonstrated using *in situ* high temperature powder X-ray diffraction (PXRD) and directed removal of some of the constituting elements. Thorough evaluation of the PXRD data yields sizes of coherently scattering domains in the nanometre-range. Transmission electron microscopy based methods support this finding and indicate a homogeneous distribution of

the elements in the samples. The combination of  $^{57}\text{Fe}$  Mössbauer spectroscopy with X-ray absorption near edge spectroscopy allowed determination of the cation occupancy on the tetrahedral and octahedral sites in the cubic spinel structure. Magnetic studies show long-range magnetic exchange interactions which are of ferri- or ferromagnetic nature with an exceptionally high saturation magnetization in the range of 92–108  $\mu\text{emg}^{-1}$  at low temperature, but also an anomaly in the hysteresis of a sample calcined at 500 °C.

## Introduction

Entropy stabilized metallic alloys have attracted increasing attention and are widely studied due to their versatile and adjustable properties.<sup>[1,2]</sup> Yeh et al. define such alloys as solid solutions containing more than five principal elements with equal or near equal atomic percentage.<sup>[3]</sup> Another definition was given by Mirakel et al. based on the entropy concept. According to this definition the requirement for an entropy stabilized compound is a  $\Delta S_{\text{mix}}$  larger than 1.61 R, where R is the

universal gas constant, 8.314 J/molK.<sup>[4]</sup> In 2015 Rost et al. extended this concept to high entropy stabilized oxides (HESO's) based on a five component rock salt structure. A configurational entropy value is generated by the random distribution of the constituent metal cations on the cation sublattice, which competes with the formation enthalpies of intermediate compounds.<sup>[5]</sup> Because the phase stability is dictated by Gibb's energy [Eq. (1)], the single-phase is stabilized with increasing temperatures and increasing number of elements, because the configurational entropy counteracts the enthalpy controlled phase separation.<sup>[6]</sup>

$$\Delta G_{\text{mix}} = \Delta H_{\text{mix}} - T\Delta S_{\text{mix}} = \Delta H_{\text{mix}} + RT \sum_{i=1}^n x_i \ln(x_i) \quad (1)$$

With  $T$  = temperature,  $\Delta H_{\text{mix}}$  = enthalpy of mixing,  $\Delta G_{\text{mix}}$  = free enthalpy of mixing,  $R$  = universal gas constant,  $x_i$  = molar concentration of each component

Rost et al. have established some requirements for such entropy controlled systems:<sup>[5]</sup>

- Low temperature equilibration should transform a single phase back to its multiphase state
- Removing components should result in a non-single phase structure at the same temperature
- The transformation from multiphase to single phase should be endothermic.

So far not only rock salt type structures have been synthesized and investigated, but also spinels,<sup>[7–17]</sup> fluorite-oxides<sup>[18]</sup> and perovskites.<sup>[19]</sup> Through entropy stabilization, novel element combinations can be obtained in an oxide phase, which may exhibit innovative physical properties. In order to design such systems, however, it is necessary to develop a deeper understanding of these complex multi-element materi-

[a] S. Senkale, Prof. Dr. W. Bensch  
Institute for Inorganic Chemistry  
Kiel University  
Max-Eyth-Str. 2, 4118 Kiel (Germany)  
E-mail: wbensch@ac.uni-kiel.de

[b] Dr. M. Kamp, Prof. Dr. L. Kienle  
Institute for Materials Science  
Kiel University  
Kaiserstr. 2, 24143 Kiel (Germany)

[c] Dr. S. Mangold  
Institute for Photon Science and Synchrotron Radiation  
Karlsruhe Institute of Technology (KIT)  
Hermann-von-Helmholtz-Platz 1,  
76344 Eggenstein-Leopoldshafen (Germany)

[d] Dr. S. Indris  
Institute for Applied Materials  
Karlsruhe Institute of Technology  
P.O. box 3640, 76021 Karlsruhe (Germany)

[e] Dr. R. K. Kremer  
Max Planck Institute for Solid State Research  
Heisenbergstrasse 1, 70569 Stuttgart (Germany)

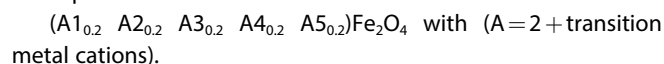
Supporting information for this article is available on the WWW under <https://doi.org/10.1002/cmtd.202200043>

© 2022 The Authors. Published by Wiley-VCH GmbH. This is an open access article under the terms of the Creative Commons Attribution Non-Commercial License, which permits use, distribution and reproduction in any medium, provided the original work is properly cited and is not used for commercial purposes.

als. Especially, spinels have a very wide range of applications, which makes them of great interest for entropic systems. Adjustable properties for, for example, catalytic oxidation or for use as DNA-based biosensors are conceivable here.<sup>[20]</sup> Different synthetic approaches have already been successfully applied to obtain entropy stabilized spinels.<sup>[7,21]</sup> The spinels reported in the literature cited above were all synthesized according to the nominal composition of the following type:



For expanding the area of spinel-based entropy stabilized solids we developed a new approach according to the following concept:



This approach has been poorly investigated so far and, in the case of iron as a trivalent cation, to the best of our knowledge just in two similar cases.<sup>[22–25]</sup> For example, Musić et al. prepared different high entropy spinels using a high temperature synthesis, which showed varying interesting magnetic properties depending on the elemental composition.<sup>[25]</sup> Hosseini Mohammadabadi et al. studied among others the magnetic and structural properties of an entropic spinel with increasing Mn content and fascinating results were obtained.<sup>[24]</sup> Despite various studies, the magnetic interactions are still not fully understood due to the complexity of occupation and oxidation states of the cations.<sup>[26–27]</sup> The first impressive studies have been performed to unravel the complex spin-electronic models.<sup>[28]</sup>

Due to the fact that in this system the equal atomic percentages only refer to the used divalent metals, evidences of entropy stabilization are provided in the present work. Since it is known that manganese-containing ferrites decompose at certain temperatures, this is a useful property to demonstrate whether an entropy stabilized spinel was obtained, since a multiphase state can be obtained that can be used to verify the first two requirements (see below).<sup>[29–31]</sup> To gain a deeper insight and understanding of the compounds, we investigated the homogeneity at the nanoscale by TEM and determined the oxidation states and the distribution of cations on the octahedral and tetrahedral sites using X-Ray Absorption Spectroscopy (XAS) and Mössbauer spectroscopy. The temperature dependent magnetic properties were also examined.

## Results and Discussion

### Influence of the amount of glucose on the particle size

A possibility to adjust the crystallite size directly during synthesis is to vary the amount of glucose. Figure 1 shows the different PXRD patterns for different glucose contents and its influence on the products after annealing at 500 °C. The more fuel is used in the combustion reaction, the smaller are the coherently scattering domains of the products. Sizes of the coherently scattering domains vary between 5 and 27 nm (determined by Rietveld refinements) while maintaining the spinel structure (Table 1). The lattice parameter increases with

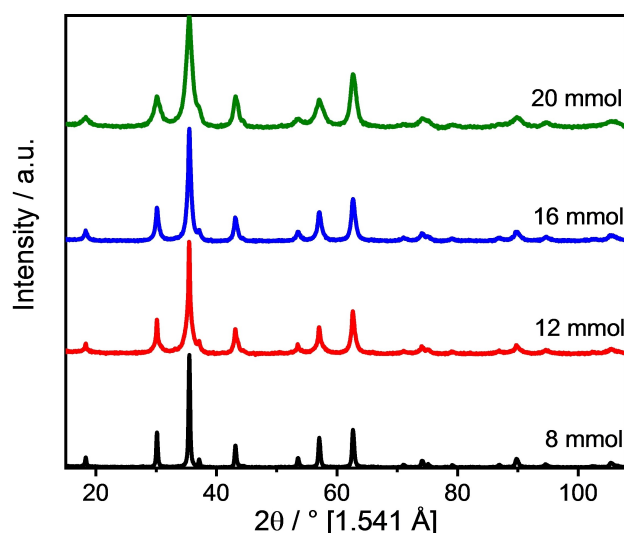


Figure 1. XRD patterns revealing the influence of the amount of glucose on the particle size.

Amount of glucose [mmol]	Crystallite size [nm]	Lattice parameter [Å]
8	27.1(3)	8.3867(2)
12	10.0(2)	8.3835(4)
16	9.7(2)	8.3843(4)
20	5.3(1)	8.376(1)

increasing particle sizes which can be explained by, for example, the high surface-to-volume ratio, stress and strain, and disorder of the constituents.

### Structural investigation of the synthesized and sintered samples of $Cu_{0.2}Co_{0.2}Mn_{0.2}Ni_{0.2}Zn_{0.2}Fe_2O_4$ (HES1)

Figure 2 shows the PXRD pattern of  $Cu_{0.2}Co_{0.2}Mn_{0.2}Ni_{0.2}Zn_{0.2}Fe_2O_4$  (HES1s) in the as synthesized (a.s.) state and the patterns of the sintered samples obtained at  $T = 500, 650, \text{ and } 1000\text{ }^\circ\text{C}$  together with the results of the Rietveld refinements. The lattice parameters and sizes of coherently scattering domains are listed in Table 2. It is unambiguous that the main fraction of the a.s. sample crystallized in the spinel-type structure with space group  $Fd\bar{3}m$ , whose lattice parameter was determined as  $a = 8.4382(2)\text{ }^\circ\text{Å}$  (similar to ICSD 184064). In addition to the spinel phase, reflections of another phase are visible and these are assigned to fcc-metals. Due to the calculated amount of 85.1% for the spinel, at least three metal species are present in this phase mixture. A Rietveld refinement including three metals gives a satisfactory result and the refined lattice parameters of 3.605(1), 3.564(1) and 3.50(1) Å can be assigned to Cu,  $\beta$ -Co and Ni. The electrochemical redox potential, XAS measurements, and magnetic properties (see below) support this assumption. A broadening of the Bragg reflections is observed presumably caused by nanosized coherently scattering domains. The sizes

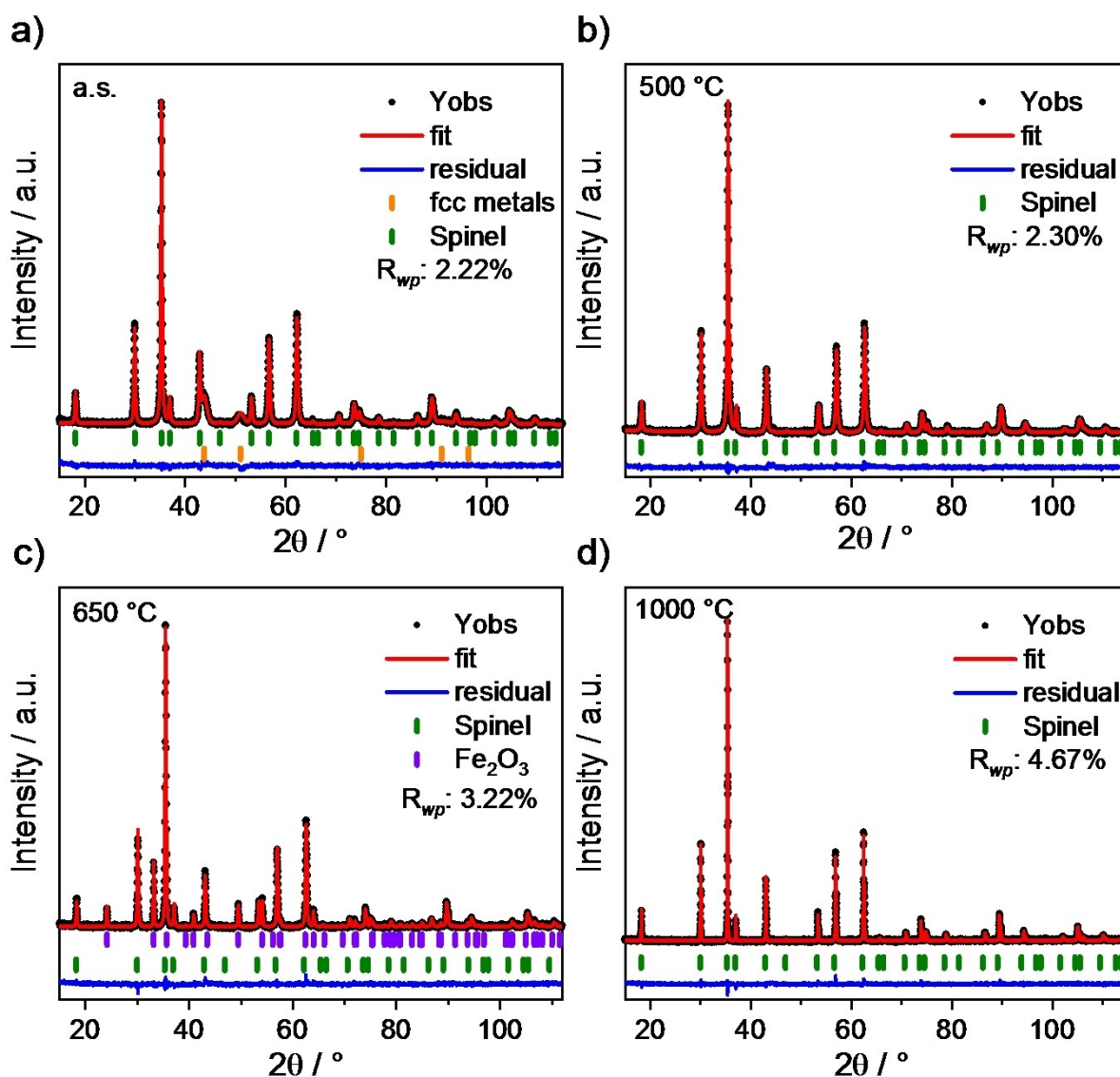


**Figure 2.** Results of Rietveld refinements against the PXR patterns of HES1s a.s.; 500 °C, 650 °C and 1000 °C. Observed (black dots), calculated (red) and difference (blue) profiles. Reflection positions are marked as vertical bars.

**Table 2.** Crystallite size and lattice constant obtained from Rietveld refinements and average crystallite size determined by TEM. Note that an average value of the lattice parameter is given for the metals in HES1 a.s. sample. Estimated standard deviations are given in parentheses.

Samples		Diameter [nm]	Weight percent [%]	Lattice parameter <i>a</i> [Å]	Diameter (TEM) [nm]	Lattice parameter (TEM) <i>a</i> [Å]
HES1s a.s.	Spinel	25.5(6)	86(1)	8.4382(2)	13.9(6)	8.52(6)
	Metals	8–10	14.9(3)	∅ 3.5814(4)		
500 °C	Spinel	27.0(3)	100	8.3867(2)	16.1(6)	8.44(6)
650 °C	Spinel	40.8(5)	79.5(2)	8.3916(1)	28.8(6)	8.52(6)
	Haematite	68(3)	20.5(2)	5.0361(4), 13.7403(6)		
1000 °C	Spinel	cryst.(176)	100	8.40668(5)	cryst.	8.44(6)

of the domains were determined to be 26 nm for the spinel phase and around 8–10 nm for the metals. As illustrated in Figure 2a the experimental pattern matches well with the refined pattern resulting in a very low value for  $R_{wp}$  of 2.22%. After heating to 500 °C, the reflections of the metals completely disappeared in the PXR pattern indicating incorporation into the spinel structure and a phase-pure spinel is obtained with

lattice parameter  $a = 8.3867(2)$  Å and a crystallite size of 27 nm (Figure 2b), similar to the size determined for the as synthesized sample. The lattice parameter is about 0.05 Å smaller than that of the a.s. sample, which could be explained either by the incorporation of the three metal species as cations and/or by a redistribution of the cations within the different tetrahedral and octahedral positions, due to this incorporation. Further heating

leads to precipitation of haematite ( $\text{Fe}_2\text{O}_3$ , ICSD 161290) at about 600 °C reaching its maximum content of ca. 20.5 wt.% at 650 °C (Figure 2c). This process is accompanied by a slight increase of the unit cell volume of the spinel and a significant growth of the domain sizes to  $\approx 41$  nm (Table 2). Another increase of the temperature results in a successive disappearance of reflections of haematite, and at about 1000 °C no reflections of this impurity can be detected (Figure 2d). At this temperature a spinel is formed with a lattice parameter of  $a = 8.40668(5)$  Å and high crystallinity. The alterations of the unit cell volume of the spinel during the heating processes are related to various effects like surface distortion of particles induced by the size effects of nanoparticles<sup>[32]</sup> as well as the distribution of cations between tetrahedral and octahedral positions.<sup>[33]</sup> The increasing interactions between the various defect-related dipoles will also have an effect<sup>[34]</sup> as well as stacking faults often observed in *fcc* materials.

Evaluation of the PDF data (see Figure S1 in Supporting Information) confirms the results obtained by the Rietveld refinements regarding domain sizes (determined by spherical damping), lattice parameters, and chemical compositions (Table 3) from samples a.s., 650 °C, and 1000 °C. The volume-averaged mean crystallite morphology could be obtained by evaluating the anisotropic broadening of the Bragg reflections. At lower temperatures the shape is almost spherical, whereas at higher calcination temperatures the shape becomes more edged (Figure S3).

The chemical composition determined by SEM-EDX analysis yields  $\text{Mn}_{0.21}\text{Co}_{0.21}\text{Ni}_{0.19}\text{Cu}_{0.20}\text{Zn}_{0.19}\text{Fe}_{2.00}\text{O}_4$  after 500 °C treatment which agrees well with the intended atomic ratios. The surface topology was investigated by using SEM images, and they indicate a certain porosity, which decreases with increasing sintering temperature (Figure S4).

### Requirements for high entropy stabilization

Rost et al. convincingly demonstrated that the system (Mg; Ni; Co; Cu; Zn)O with rocksalt structure is entropy stabilized and we performed the same experiments to verify the entropy stabilization of the spinel. To demonstrate reversibility, which is a basic requirement for entropy driven systems, the as synthesized sample was heated in an oven between 27 and 900 °C and the changes were monitored with in situ PXRD (Figure 3a). The selected Bragg angles from 29 to 34° 2 $\theta$  represent a good range to show the structural changes. At the beginning just the reflections of the spinel and the reference material  $\text{ZrO}_2$  are

**Table 3.** Crystallite size and lattice parameters obtained from PDF refinements. Estimated standard deviations are given in parentheses.

Samples		Diameter [nm]	Lattice parameters [Å]
HES1s a.s.	Spinel	30	8.4509(1)
	Metals	5	3.5832(4)
HES1s 650 °C	Spinel	49	8.4030(1)
	Haematite	63	5.0458(8), 13.763(4)
HES1s 1000 °C	Spinel	Cryst.	8.4098(1)

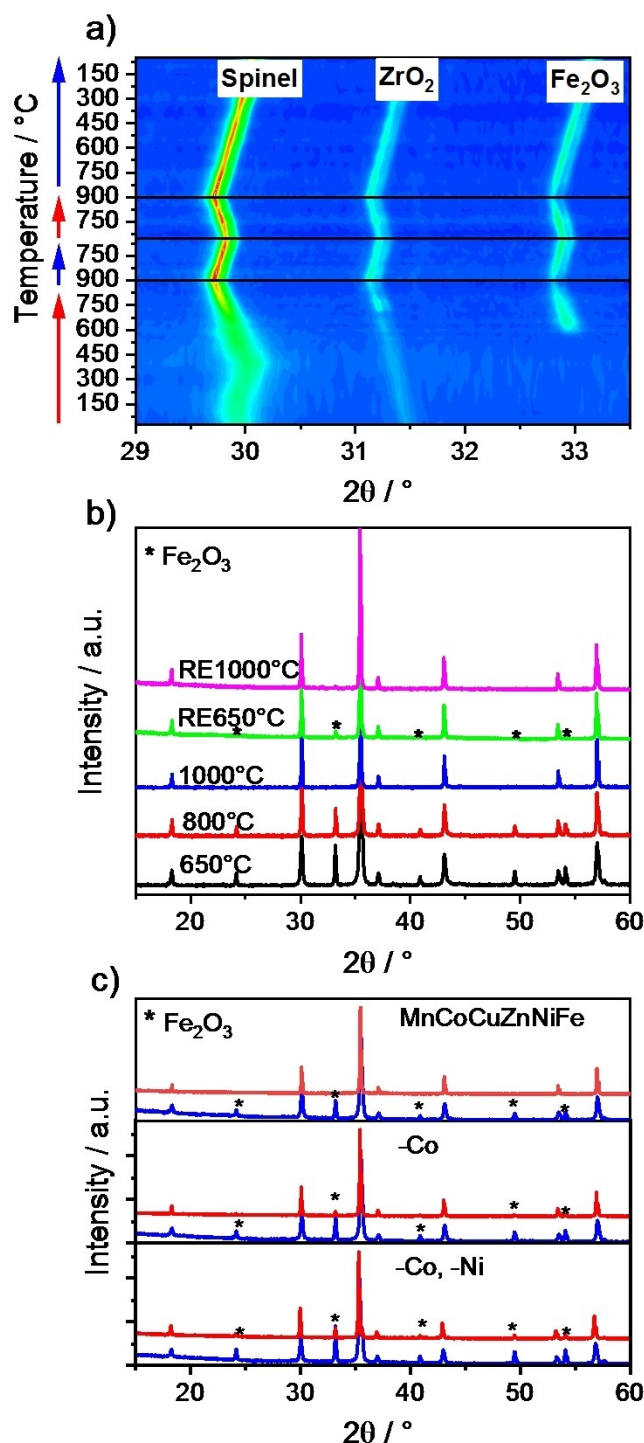


**Figure 3.** a) In situ XRD intensity map as a function of 2 $\theta$  and temperature; note that  $\text{ZrO}_2$  is used as reference material b) Ex situ XRD analysis of samples heat-treated at different temperatures (RE for returned to). c) removal of components from the initial material and heat treatments at 650 °C (blue) and 1000 °C (red).

visible. Further heating to  $T = 650$  °C led to the development of reflections of  $\text{Fe}_2\text{O}_3$  like observed during the ex situ experiments. With increasing temperature, the intensity of the reflections of  $\text{Fe}_2\text{O}_3$  is significantly reduced until they are hardly detectable at 900 °C. When the sample is cooled down, the

intensity of reflections of  $\text{Fe}_2\text{O}_3$  significantly increases again. Hence, the reversibility of this reaction is impressively demonstrated. Due to the temperature limitation of our in situ stage we were not able to heat to temperatures higher than  $900^\circ\text{C}$ , and therefore an additional ex situ experiment was performed (Figure 3b). It is obvious that heating to  $1000^\circ\text{C}$  leads to formation of a phase pure spinel phase. Low temperature equilibration at  $650^\circ\text{C}$  (Figure 3b, RE650 $^\circ\text{C}$ , green pattern) transforms the spinel back into the multiphase state and annealing of this phase mixture at  $1000^\circ\text{C}$  again (Figure 3b, RE1000C, pink pattern) results in crystallization of a single-phase spinel.

Another requirement for entropy-stabilized samples is that removing single components from the mixture results in an

increase of the transition temperature for the transformation into the phase-pure product due to the lowered entropy. Removing either Co or Co/Ni it can be undoubtedly demonstrated that at  $1000^\circ\text{C}$  no single-phase product is obtained due to the increased transition temperature, which additionally proves the entropy stabilization of our system (Figure 3c).

### TEM investigations

The combination of different TEM methods (HRTEM, SAED and STEM-EDX) was mainly used to study the homogeneity of HES1 samples at  $500^\circ\text{C}$  and  $1000^\circ\text{C}$ . An overview TEM image in Figure 4a displays the crystallite sizes of the HES1  $500^\circ\text{C}$

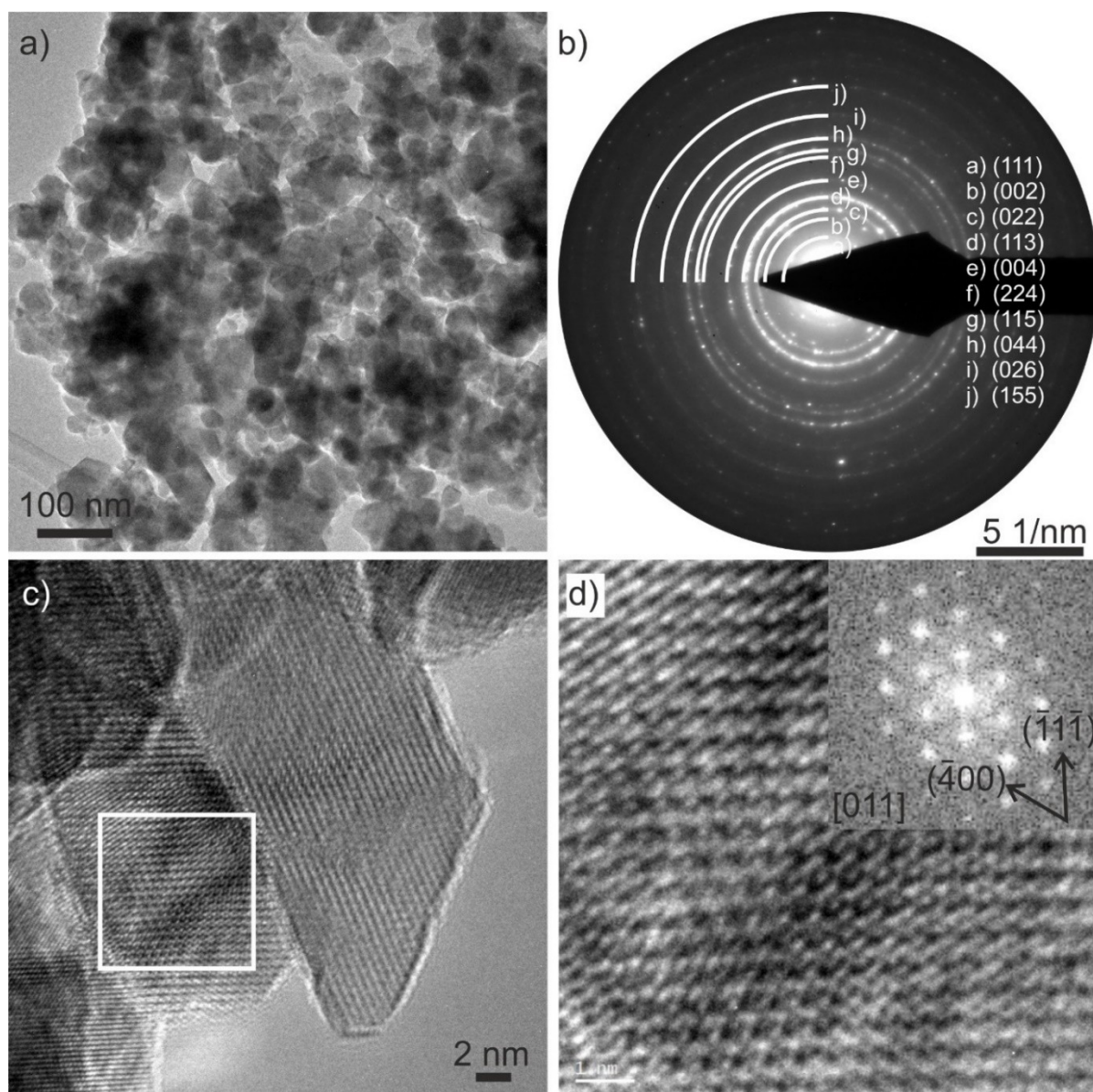


**Figure 4.** TEM analysis of HES  $500^\circ\text{C}$  sample, a) TEM image shows agglomeration of the powder. b) Reflection intensity on concentric rings in the SAED pattern can be assigned to a spinel phase (described before), the respective crystallographic planes are marked. The crystal structure was verified by c) an HRTEM micrograph showing different crystallites (the marked area is magnified in d)) and d) a magnified HRTEM micrograph with a fast Fourier transform indicating the spinel phase in a  $[110]$  zone axis orientation.

sample. The respective SAED pattern (Figure 4b) from the same sample position shows reflection intensity on concentric rings that can be assigned to a single-phase spinel structure. In particular, no reflection intensities of additional phases such as copper, cobalt, or nickel were observed. The spinel phase formation was verified by HRTEM and respective fast Fourier transforms (Figure 4c and d), showing a pattern that indicates the spinel phase crystallites in the [011] zone axis. However, the STEM-EDX elemental mapping (Figure S5 and S6) evidences an inhomogeneous distribution of the Cu signal, while the Zn, Mn, Co, Fe, and O signals are homogeneously distributed. This observation indicates partial segregation of Cu, however, the absence of reflection intensities of elemental Cu suggests the formation of an amorphous phase (e.g.,  $\text{CuO}_x$  or  $\text{CuO}_x\text{H}_y$ ). It is possible that the segregation of a Cu phase might be induced by the electron beam during STEM-EDX elemental mapping. Figures S6b and S6c show the sample after electron beam irradiation with obvious contrast variations in HAADF-STEM and TEM imaging, respectively. The absence of reflection intensities of a Cu phase before (Figure S6d) and after (Figure S6e) beam irradiation suggests the formation of an amorphous Cu-rich phase. These Cu-rich precipitates can be intrinsic to the sample or formed by the electron beam. In both cases, their amorphous structure would explain why they are not evident in XRD.

The TEM investigation of the HES1 1000 °C sample demonstrates the presence of the spinel phase with a large crystallite size, which is verified by SAED and HRTEM micrographs. A SAED pattern in the  $[-14-1]$  zone axis and a HRTEM micrograph with a Fourier transform in the [130] zone axis is depicted in Figure 5a) and b), respectively. STEM-EDX elemental mapping (c) indicates a homogeneous distribution of all elements on the given scale, without the partial segregation of Cu, which was observed for the HES1 500 °C sample. This observation might be attributed to the large crystallite size of the HES1 1000 °C sample.

Furthermore, dark-field TEM imaging can be used to obtain crystallite size distributions of all four HES1s samples. In dark-field TEM the randomly distributed crystallites partially fulfill the Bragg condition resulting in bright contrast of the crystallites in the images. The increase of average crystallite size with the increasing sintering temperature verifies the results from the Rietveld refinements (Table 2). The histograms (Figure S7) are fitted with a Lognormal distribution function which gives an average crystallite size of  $13.9 \pm 0.2$  nm,  $16.1 \pm 0.6$  nm, and

$28.8 \pm 1.4$  nm for the HES1 a.s., 500 °C, and 650 °C samples, respectively. In accordance to the results of the Rietveld refinement, the HES1 1000 °C sample shows an almost single crystalline structure (crystallite size  $> 150$  nm).

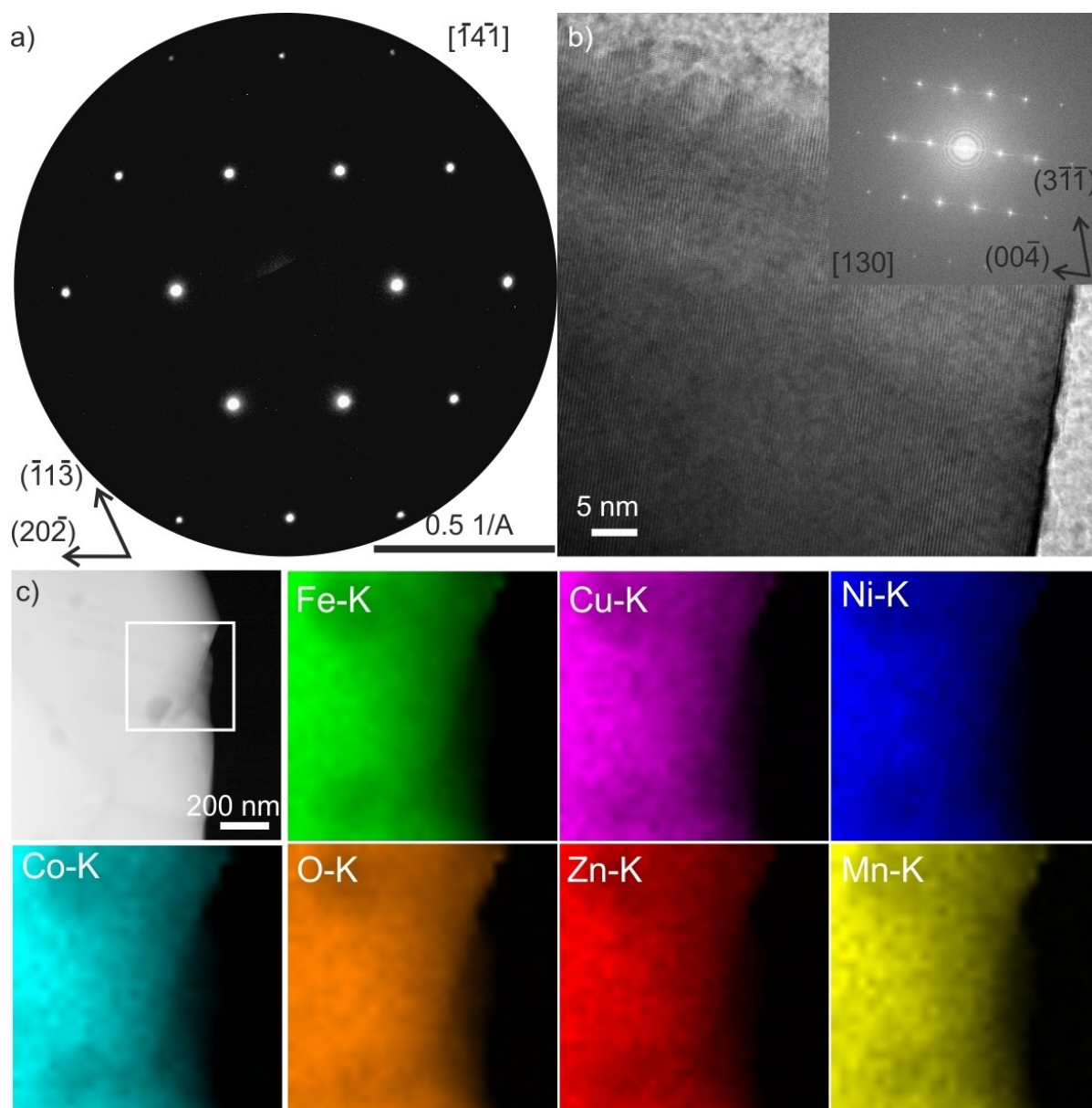
#### Determination of $\text{Fe}^{2+/3+}$ distribution with Mössbauer spectroscopy

Figure 6 shows the room-temperature  $^{57}\text{Fe}$  Mössbauer spectra of the high-entropy spinel oxides. The sample heated to 1000 °C clearly shows a sextet pattern revealing magnetic ordering in the spinel structure, even at room temperature. The broad lines in this sextet show an asymmetry that can be described either by superposition of multiple sextets or by a distribution of hyperfine fields. A reasonable fit can be achieved with two sextets with isomer shifts (IS) of 0.29 mm/s and 0.36 mm/s, respectively (Table 4). These values evidence that exclusively trivalent  $\text{Fe}^{3+}$  is present in the sample. The values of the quadrupole splitting (QS) for the two spectra (Table 4) undoubtedly support the assignment of  $\text{Fe}^{3+}$ . The hyperfine field of the major sextet (68%) amounts to 47.8 T, while that of the minor sextet (32%) is 44.0 T. Similar values have been reported for  $\text{MgFe}_2\text{O}_4$ <sup>[35]</sup> while for  $\text{MnFe}_2\text{O}_4$  slightly larger hyperfine fields have been observed.<sup>[36]</sup> This is reasonable since  $\text{MnFe}_2\text{O}_4$  contains a larger concentration of paramagnetic cations in comparison to the high-entropy spinels. The broad lines (see  $\Gamma$  values in Table 4) in these sextets and the asymmetry of the single lines are caused by the mixing of the multiple metal ions on the different cation sites in the spinel structure resulting in many different next-nearest neighbor environments around the  $\text{Fe}^{3+}$  cations. The intensity ratio of 2:1 suggests a random distribution of  $\text{Fe}^{3+}$  ions on the octahedral and tetrahedral sites of the spinel structure.

The sample heated to 650 °C also shows these two contributions, with similar values for IS,  $\Gamma$ , QS, and a similar intensity ratio of about 2:1 (Table 4). In addition, a third sextet contribution is clearly visible (blue sextet in Figure 6) with IS = 0.37 mm/s, QS = -0.23 mm/s, and a hyperfine field  $B_{\text{hf}}$  of 51.4 T. These values are consistent with the presence of  $\alpha\text{-Fe}_2\text{O}_3$  (hematite),<sup>[37]</sup> in accordance with the PXRD results discussed above. Again, only trivalent  $\text{Fe}^{3+}$  is present in this sample. It is interesting to note that the splitting of the main sextets is reduced in the sample heated to 650 °C ( $B_{\text{hf}}$  = 46.4 and 42.2 T,

**Table 4.** Fit parameters used to describe the Mössbauer spectra of the high-entropy spinel oxides: isomer shift (IS), quadrupole splitting (QS), hyperfine field ( $B_{\text{hf}}$ ), line width ( $\Gamma$ ), and area fraction. IS, QS, and  $\Gamma$  are given in mm/s.  $B_{\text{hf}}$  is given in T. Note that the second fitted contribution of the spectrum of the a.s. sample represents the modelling of the background.

sample	IS	QS	$B_{\text{hf}}$	$\Gamma$	area frac.
500 °C	0.289(1)	-0.007(2)	47.2(1)	0.608(5)	67.8%
	0.333(5)	-0.055(9)	43.2 (1)	1.01(2)	32.2%
650 °C	0.281(2)	-0.010(4)	46.4(1)	0.62(1)	50.0%
	0.341(8)	-0.08(2)	42.2(1)	1.02(3)	25.6%
	0.371(1)	-0.231(3)	51.4(1)	0.324(5)	24.4%
1000 °C	0.287(1)	-0.006(1)	47.8(1)	0.568(3)	68.2%
	0.355(3)	-0.046(7)	44.0(1)	0.95(1)	31.8%
a.s.	0.336(2)	0.771(3)	-	0.904(8)	45.8%
	0.250(2)	$7.094 \pm 0.135$	-	8.0(4)	54.2%



**Figure 5.** TEM analysis of the HES 1000 °C sample: a) SAED pattern in  $[-1\ 4\ -1]$  zone axis verifies the one-phase spinel formation with large ( $> 150$  nm in diameter) crystallite sizes, underlined by a HRTEM micrograph and a fast Fourier transform from a single crystallite with  $[1\ 3\ 0]$  zone axis orientation. c) STEM-EDX elemental mapping shows a homogeneous distribution of the elements, darker contrast in the HAADF-STEM-image seems to be based on thickness variation.

cf. Table 1) compared to the phase obtained at 1000 °C (47.8 and 44.0 T), probably due to the loss of some Fe in the spinel phase caused by the formation of  $\alpha$ - $\text{Fe}_2\text{O}_3$ .

The spectrum of the material heated to 500 °C is very similar to that of the sample annealed at 1000 °C and gives almost identical fit parameters (Table 4). The fact that the intensity ratio of the two sextets of the main phase (dark red and light red sextets in Figure 6) is always 2:1 for all sintering temperatures (500 °C, 650 °C, and 1000 °C) reveals that Fe cations forming hematite are removed from both crystallographic sites at 650 °C and they are also reinserted on both sites at 1000 °C.

The spectrum of the as-prepared sample shows a doublet with isomer shift  $IS = 0.34$  mm/s and quadrupole splitting  $QS =$

0.77 mm/s. The IS value reveals  $\text{Fe}^{3+}$  ions on the octahedral sites in the spinel structure. The large line width of this doublet ( $\Gamma = 0.90$  mm/s) again shows the good mixing of the multiple metal ions around the  $\text{Fe}^{3+}$  ions. The fact that only a doublet can be observed in this case shows that a magnetic ordering does not occur in the nanocrystalline sample at room temperature. This might be caused by a broad distribution of crystallite sizes, and at least for some fraction of the sample the small crystallite sizes seem to lower the Curie temperature, as it was observed earlier for other nanocrystalline materials.<sup>[38,39]</sup> A broader background contribution in this spectrum is described with a second doublet with large splitting and large line width of the single lines. This broad component reveals the poor

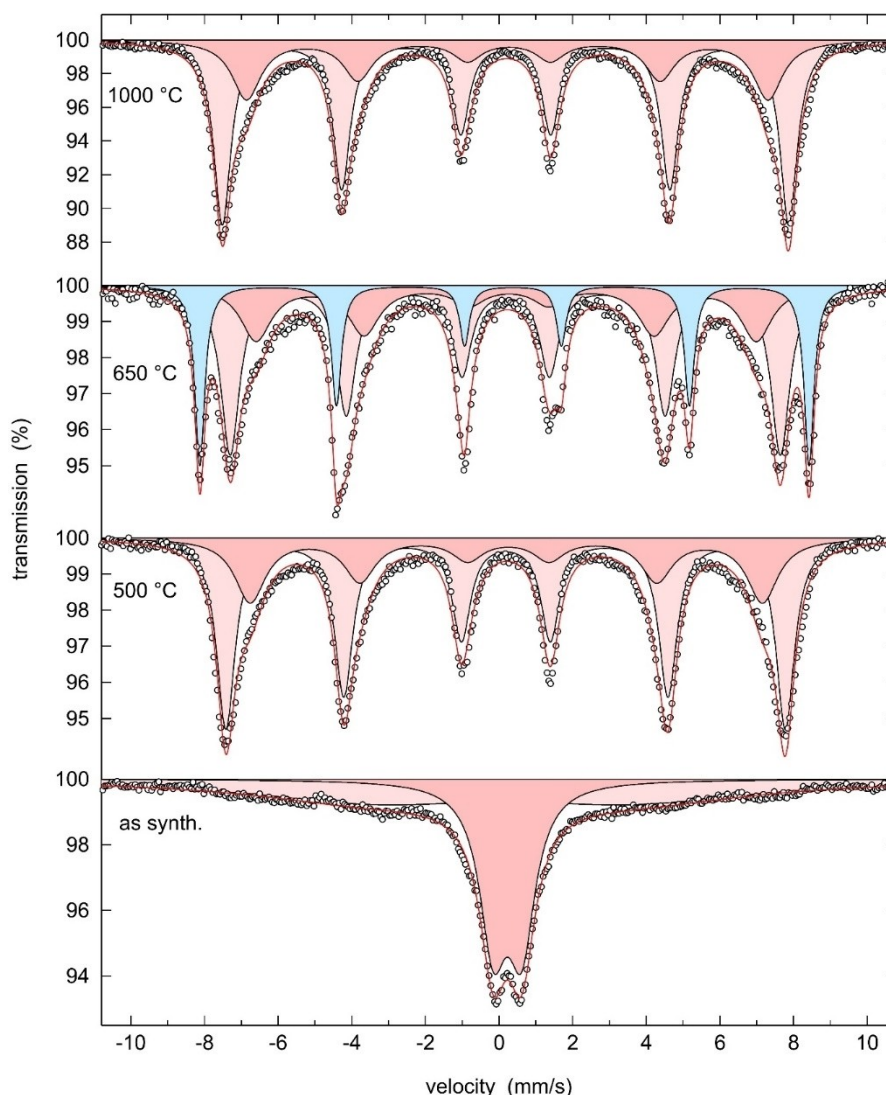


**Figure 6.**  $^{57}\text{Fe}$  Mössbauer spectra of the as-synthesized high-entropy spinel oxide and the samples heated to 500 °C, 650 °C, and 1000 °C. The experimental data points are shown as white spheres, the overall fit as red line, and the subspectra are shown as blue and red doublets/sextets.

crystallinity of this sample and the high degree of disorder. Furthermore, the presence of metallic Ni and Co particles might result in a large variation of local magnetic fields.

Since the crystallite size of the 500 °C sample differs only slightly from that of the a.s. sample, these results confirm that the incorporation of the metals -still present in elemental form in the a.s. sample- drastically changes the magnetic properties (see section 2.7).

The random distribution of  $\text{Fe}^{3+}$  also supports the assumption of an entropy stabilized spinel.

#### Investigation of the local environments via X-ray absorption spectroscopy

The XAS results will be discussed in more detail per element in the XANES and EXAFS region. While the XANES region will be used to extract the oxidation state, the structural information

will be extracted by using the EXAFS part. The edge position in comparison to reference spectra with well-known oxidation state can be used to get information about average oxidation states in the respective sample. As expected the lower R-region in the Fourier transform (FT) is for most of the samples with oxidation state larger than zero and a nearest neighbor oxygen pretty similar. The region from 2.2–3.5 Å gives valuable information about the environment of the metal cations in the spinel. An octahedral coordination will show two peaks, the tetrahedral coordination only one significant peak at a higher R-value (Figure 7).

#### The Mn K-edge region

The edge position of the XANES spectra (Figure 8a) indicates an average oxidation state of three for HES1s a.s. and HES1s 1000, while it is slightly larger for HES1s 500 and 650 ( $3.5 \pm 0.2$ ).

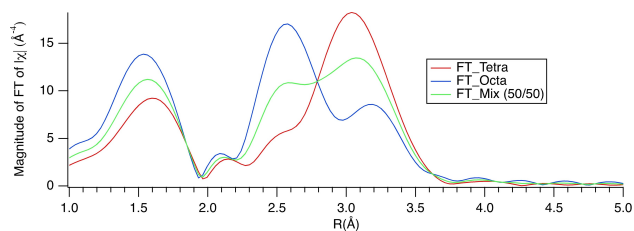


**Figure 7.** Simulated Fourier Transform (FT) spectra for a backscatter atom in tetrahedral or octahedral crystallographic site in the spinel structure and the spectrum for the mixed case.

The EXAFS spectra show a more complex picture (Figure 8a). In the HES1s 500 and 650 samples Mn cations are mainly

octahedrally coordinated, while in HES1s 1000 may be a half-half mix of octahedral and tetrahedral coordinated Mn atoms are present (Figure 8b, compare also Figure 7).

### Fe K-edge region

The edge position of the XANES spectra indicates an average oxidation state of three for all samples, and only the Fe cations in HES1s 500 may have a slightly lower oxidation state (Figure 8c).

For HES1s 650 most of the Fe cations seem to be located on octahedral sites (more than 80%) and for the remaining samples a distribution of  $\approx 2/3$  on octahedral and  $\approx 1/3$  on tetrahedral sites is observed, that is, a random distribution of Fe

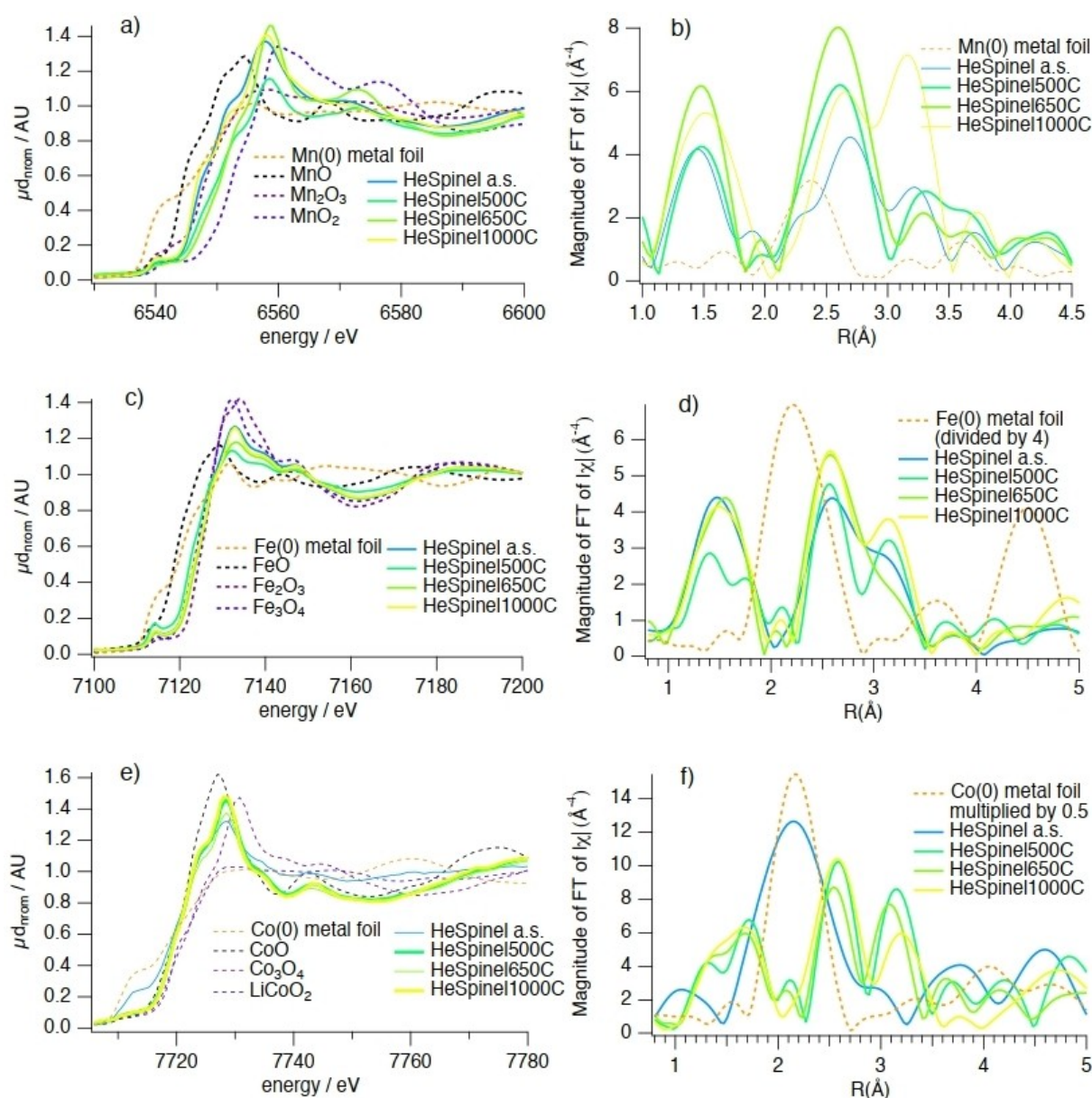


**Figure 8.** The XANES region of the a) Mn K-edge c) Fe K-edge and e) Co K-edge of the spin samples and of selected reference compounds for comparison; b), d) and f) R-region of the corresponding samples and metal foils (b) Mn, d) Fe, f) Co).

on the available sites. The limited possible measurement range and a Si111 crystal glitch do not allow a more detailed analysis. The oxidation state of 3+ and the random distribution of Fe on tetrahedral/octahedral sites are in good agreement with the Mössbauer results described above.

### Co K-edge region

Figure 8e demonstrates that the Co K-edge position of the XANES spectra indicates an average oxidation state of two or slightly higher for samples HES1s 500, HES1s 650, and HES1s 1000. The sample HES1s a.s. contains 2/3 Co in oxidation state zero and 1/3 in oxidation state 2+. The FT of the HES1s a.s. is in good agreement with the XANES results. The blue curve in Figure 8f shows a broad peak together with three additional peaks: one at low R value and two at high R values. The centre of the broad peaks matches with that of the metallic Co foil, that is, it represents the typical Co–Co distance. While the HES1s 1000 sample has a slightly lower amount of occupied tetrahedral sites, the Co atoms in HES1s 500 and 650 show 2/3 octahedral and 1/3 tetrahedral coordination.

### Ni K-edge region

The extractable information for the XANES at the Ni K-edge is very similar to that for the Co K-edge. The Ni K-edge position of the XANES spectra indicates an average oxidation state of +2 or slightly higher for samples HES1s 500, HES1s 650, and HES1s 1000. The sample HES1s a.s. consists of 2/3 Ni in oxidation state zero and 1/3 oxidation state 2+ (Figure 9a).

Due to the longer measurable k-range the extractable information of the FT shows much more details compared to the Mn and Fe K-edges. For HES1s 500, HES1s 650, and HES1s 1000 Ni is mainly in an octahedral coordination in the FT. The FT of the HES1s a.s. is in perfect agreement with the XANES results. The violet curve in Figure 9b shows a broad peak with a shoulder at low and high R values, and the centre of the main and broad peak matches with that of metallic Ni evidencing the presence Ni(0) particles.

### Cu K-edge region

The XANES spectra at the Cu K-edge can be interpreted similar to those of Ni and Co. A mixture of  $\approx 2/3$  Cu<sup>0</sup> and  $\approx 1/3$  Cu<sup>2+</sup> is

present in HES1s a.s., while for the remaining samples the average oxidation state is +2 (Figure 9c). The octahedral coordination of Cu<sup>2+</sup> is evidenced by the two signals located at  $\approx 1.4$  and  $\approx 2.6$  Å in the FT (Figure 9d) for HES1s 500, HES1s 650, and HES1s 1000. The presence of  $\approx 2/3$  metal environment is clearly detected in the FT of HES1s a.s. as the intense signal at  $\approx 2.2$  Å matches with that of the Cu foil. The remaining  $\approx 1/3$  Cu<sup>2+</sup> cations are most probably in an octahedral coordination environment.

### Zn K-edge region

The XANES spectra of all samples agree well with the presence of most Zn atoms in the oxidation state 2+ (Figure 9e). In contrast to the other elements, the Zn<sup>2+</sup> cations are solely in a tetrahedral coordination as can be extracted from the FT curves shown in Figure 9f. The HES1s a.s. shows a much lower peak intensity, which may indicate very small particles.

### Magnetic properties

Magnetic hysteresis loops were measured at room temperature and at 5 K up to 90 kOe, which are displayed in Figure 10. In addition, zfc/fc curves were collected at H=250 and 1000 Oe from 293 to 2 K (Figure 11). The relevant parameters extracted from the hysteresis loops such as maximal magnetization ( $M_m$ ), remanent magnetization ( $M_R$ ) and coercivity ( $H_C$ ) are listed in Table 5.

The magnetization curves collected at 5 K of the as synthesized sample already exhibits hysteresis. The coercive fields markedly increase for the 500 °C and the 650 °C annealed samples indicative of substantial ferri- or ferromagnetic anisotropy, whereas magnetic hysteresis for the sample annealed at 1000 °C decreases and almost vanishes, resembling a soft ferromagnetic behaviour (Figure 10a–d). The coercive fields correlate with the crystallinity of the sample. For the 500 °C, 650 °C, and 1000 °C samples Figure 11 reveals a linear increase of the coercive fields as a function of the inverse average crystallite size (see Table 2), that is, the smaller the average crystallite size the larger is the coercive field (see Equation (4)).

For all samples hysteresis disappears at room temperature (Figure 10a–d). For the a.s. and the 500 °C sample full saturation cannot be reached even at the largest external magnetic field which is a hint to magnetic frustration and/or a very large crystalline anisotropy, which may be associated with substantial

**Table 5.** Magnetic properties of the as synthesized sample and samples sintered at 500 °C and 1000 °C.

sample	T [K]	$M_m$ [emu/g]	Magnetic moments [ $\mu_B$ ]	$H_C$ [Oe]	$M_R$ [emu/g]	$K \cdot 10^3$ [erg/g]
a.s.	5	60.9	2.6	824.3	16.8	52.3
	300	46.5	2.0	29.2	1.2	1.4
500 °C	5	92.6	3.9	2414.4	56.9	232.9
	300	71.2	3.0	50.1	5.5	3.7
1000 °C	5	107.7	4.6	101.8	12.2	11.42
	300	81.2	3.4	6.4	0.9	0.5

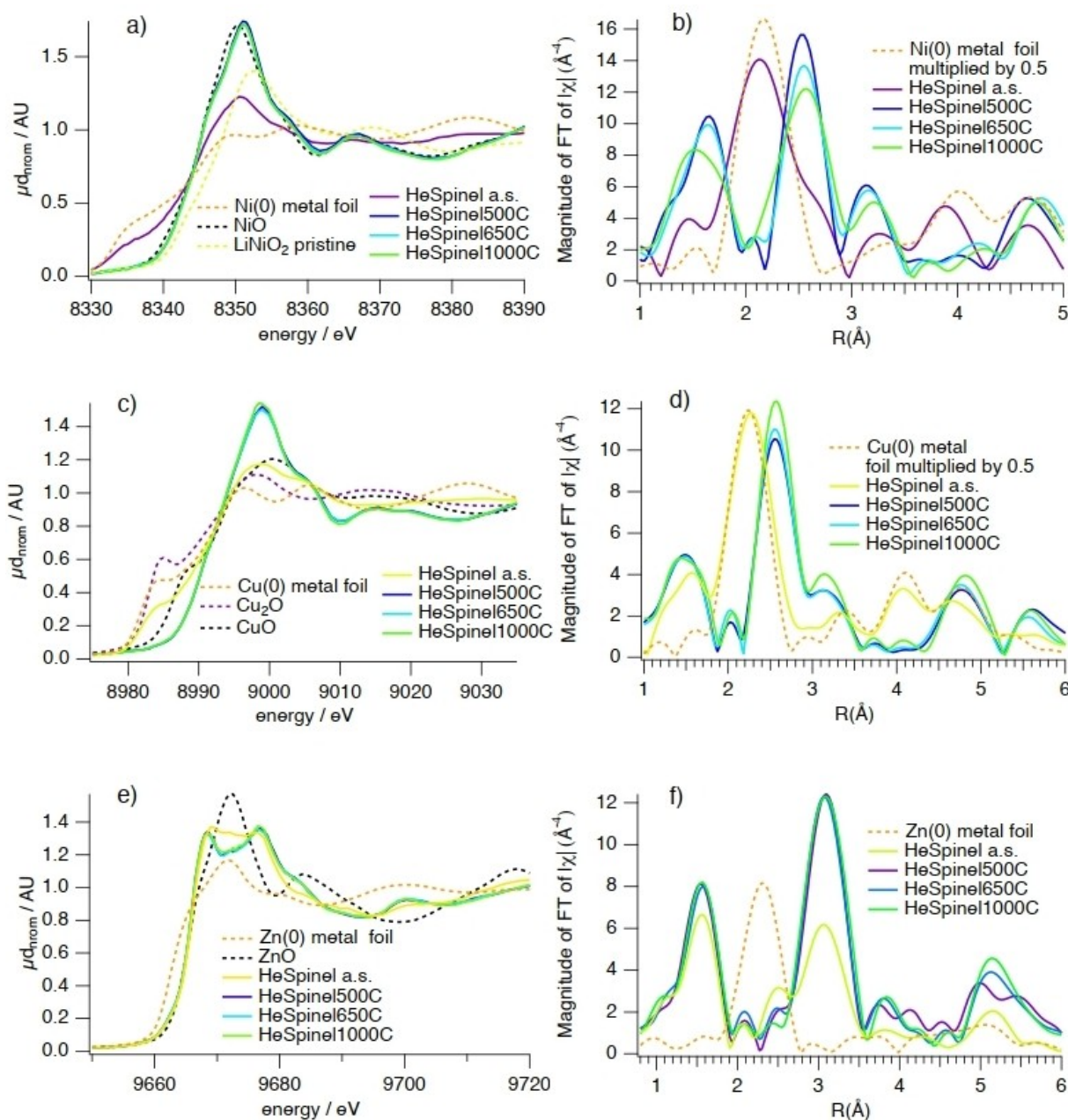


**Figure 9.** The XANES region of the a) Ni K-edge c) Cu K-edge and e) Zn K-edge of the spinel samples and of selected reference compounds for comparison; b), d) and f) R region of the corresponding samples and metal foils (b) Ni, d) Cu, f) Zn).

surface disorder of the crystallites.<sup>[40–42]</sup> The shape of the hysteresis curves of the a.s. samples can possibly be attributed to the presence of two different magnetic contributions, one of the spinel and a softer contribution which we tentatively assign to a minor phase or to intrinsic structural inhomogeneity. For the a.s. sample it is highly likely that the cation distribution is inhomogeneous at the atomic level and one may assume that different small magnetic regions coexist. In addition, nanoparticles are prone to structural defects which also affect the magnetic properties. Impact of Co and Ni metallic nanoparticles to the observed behaviour may also be considered. The value of  $M_M$  (Figure 10a) at  $H=90$  kOe is estimated to be  $60.1 \text{ emu g}^{-1}$

at 5 K. But taking into account that  $\approx 15\%$  of the phase mixture consists of the metals Co, Ni, and Cu of where only Cu is non-magnetic, the real value for  $M_M$  of the spinel phase cannot be seriously estimated. The values for  $H_C$  and  $M_R$  indicate that the ferri-/ferromagnetic components are soft magnets. After heating the sample to  $500^\circ\text{C}$  (Figure 10b) slight changes of the shape of the hysteresis loop are seen and like for the as synthesized sample two magnetic components seem to contribute to the hysteresis. Initial considerations suggested that an impurity of hematite, not visible in the XRD data, is responsible for this anomaly. However, the hysteresis loop of the  $650^\circ\text{C}$  sample demonstrates that this is not the case and the origin

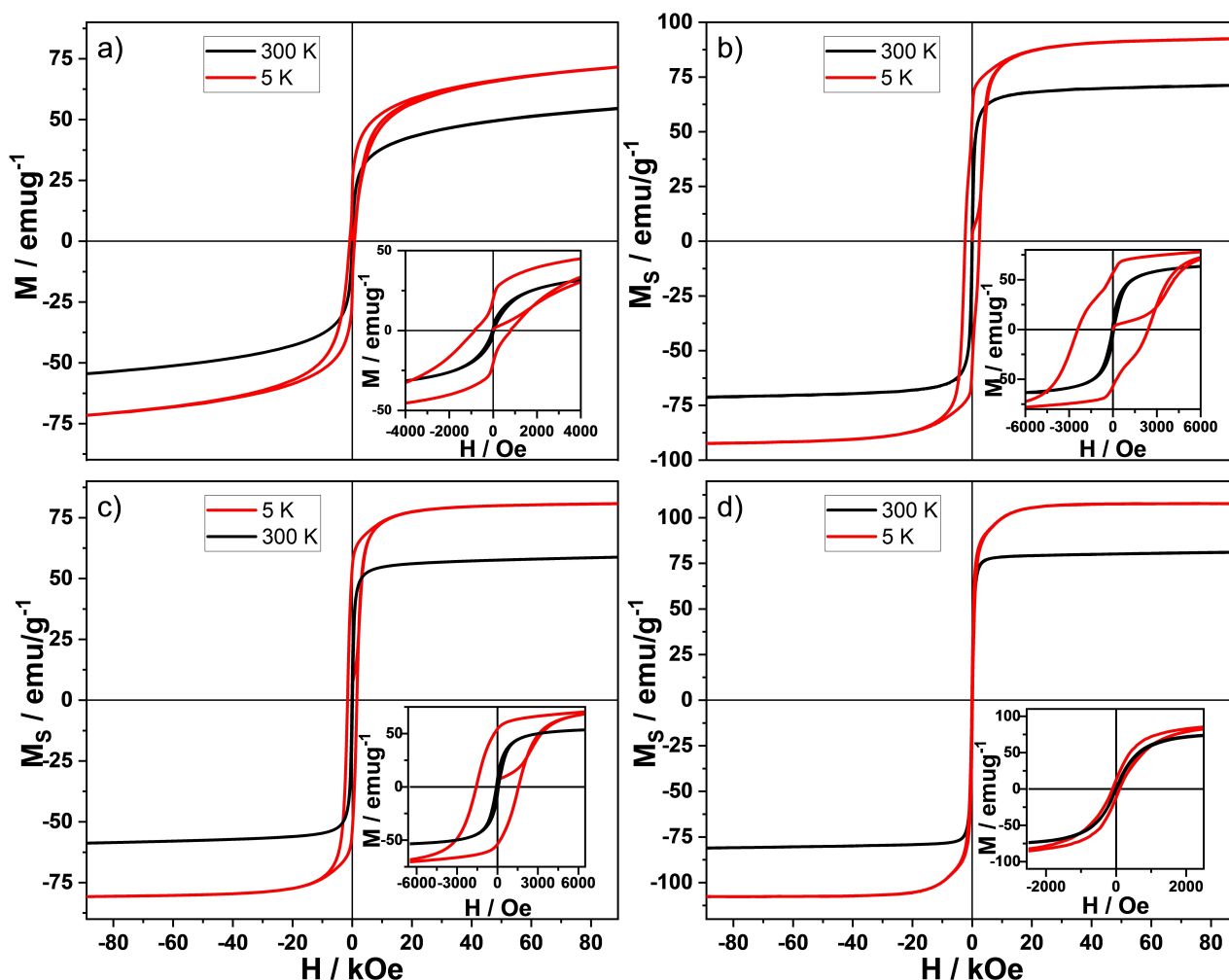


Figure 10. Magnetic hysteresis loops of a) HES1 a.s., b) HES1 500 °C, c) HES1 650 °C and d) HES1 1000 °C at 300 K (black) and 5 K (red), the inset shows the coercivity region.

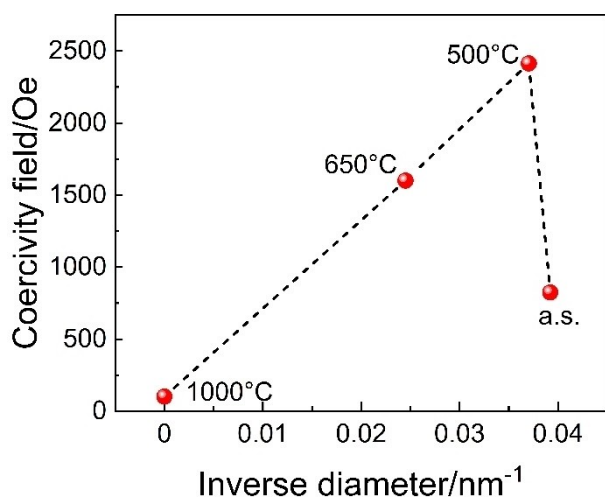


Figure 11. Diagram of linear dependence of the coercivity field versus inverse average crystallite size.

must be different (Figure 10c). Since the crystallite size of the a.s. and 500 °C samples is still on the nanoscale with 25 and

27 nm, respectively, and the crystalline order is still not well developed, magnetic domain effects could also be responsible for the shape of the hysteresis curve (also for the a.s. sample). The splitting of the zfc-fc curve of the 500 °C sample occurs at much higher temperature than for the 1000 °C sample indicating a pronounced domain pinning, and taking into account domain rotations the shape of the hysteresis curve is caused by these effects. Like for the a.s. sample the  $M(H)$  cycle is not closed at low magnetic fields up to  $\approx 11$  kOe, that is, the magnetic irreversibility is still present but clearly reduced compared to the a.s. sample. In the highest field the hysteresis curve of the 500 °C sample is almost indicating reduction of the surface spin disordered layer and/or of the magnetic frustration. These effects as well as the incorporation of Co, Ni, and Cu into the spinel, which may result in a redistribution of the cations to the tetrahedral/octahedral sites, contribute to the increase in  $M_M$  to  $92.6 \text{ emu g}^{-1}$ . We note that this is an exceptionally high saturation magnetization for 27 nm particles. The strong increase in coercivity from 1648 to 4827 Oe may also be explained by incorporation of Co and Ni into the spinel structure because especially cobalt ferrites possess a high

magnetic anisotropy.<sup>[43,44]</sup> The precipitation of hematite leads to a slight decrease of the saturation magnetization, which is more pronounced at 5 K, which is quite conclusive due to the magnetic behavior of hematite (Figure 10c).<sup>[45]</sup>

Sintering at 1000 °C leads to much larger particles and a larger  $M_M$  of 107.7 emu/g (Figure 10c). In contrast to the other samples the M(H) curve is now closed suggesting the removal of magnetic irreversibility. Possible explanations for the enhanced  $M_M$  are the reduction of surface effects such as spin canting as evidenced by saturation of the magnetization at relatively low magnetic fields and/or the higher crystallinity, better cation ordering and lower amounts of structural defects.<sup>[42]</sup> For spinels with general formula  $AB_2O_4$  three different superexchange interactions mainly contribute to the net magnetization: A–A, B–B and A–B with the latter being the strongest one. The B–B interaction is antiferromagnetic but less strong than the ferromagnetic A–B exchange. Hence, the increased value for  $M_M$  indicates a redistribution of the cations over the tetrahedral and octahedral sites strengthening the magnetic exchange interactions.

The calculated magnetic moments using Equation (2) increase from 2.6 to 3.9  $\mu_B$  (Table 5).<sup>[46]</sup>

$$\mu_s[\mu_B] = M_M \left[ \frac{\text{emu}}{\text{g}} \right] \times M_{\text{mol}} \left[ \frac{\text{g}}{\text{mol}} \right] / 5585.8 \left[ \frac{\text{emu}}{\text{mol}} \right] \quad (2)$$

where  $\mu_s$  = magnetic moments,  $M_M$  = maximal magnetization and  $M$  = molecular weight

These  $M_M$  values are significantly higher than those reported for ferrites containing divalent transition metal cations (Table 6) indicating a better exchange interaction.

The coercivity is strongly dependent on the particle size and in the single domain region it decreases with increasing particle size according to Equation (3),<sup>[55]</sup>

$$H_c = a + \frac{b}{D} \quad (3)$$

where  $a$  and  $b$  = constants and  $D$  = diameter of the particle, while in the multi-domain region it decreases with increasing particle size according to Equation (4):

$$H_{ci} = g - \frac{h}{D^{3/2}} \quad (4)$$

where  $g$  and  $h$  = constants and  $D$  = diameter of the particle

This explains the decrease in coercivity with increasing crystallite size and proves that the multi domain state dominates (see also Figure 11).<sup>[43]</sup>

The total magnetic anisotropy constant  $K$  (see Table 5) was calculated via Equation (5).<sup>[56]</sup>

$$K = \frac{M_s \times H_c}{0.96} \quad (5)$$

But the values for  $K$  should be considered as a first estimate because the Stoner–Wohlfahrt model is only applicable if the magnetic nanoparticles do not interact.

For the as synthesized sample the zfc-fc curves show a clear splitting for both applied magnetic fields (Figure 12a). Next to nanosized metal particles, the spinel type material is the main fraction and one can assume that the crystallites of the spinel phase dominate the magnetic anisotropy behaviour. For the 500 °C sample the magnetic anisotropy is even larger than for the as synthesized sample, which is reflected in the zfc-fc curves where the magnetic anisotropy field significantly influences the shape of the curves. A small magnetic field is applied after zfc and due to the large magnetic anisotropy, the magnetization is low until there is enough thermal energy to overcome the energy barrier for alignment of the spins (Figure 12b). Hence, a large splitting of the zfc and fc curves occurs for the 500 °C sample. The blocking temperature  $T_B$  and the curve splitting at irreversible temperature  $T_{irr}$  (the largest size of unblocked particles) were determined to be 273 and 297 K, respectively. In contrast to many superparamagnetic materials the zfc curve does not pass a well pronounced cusp and the broad maximum indicates a wide energy barrier distribution. The high thermomagnetic irreversibility (TMI) evidenced by the strong divergence between the zfc and fc curves in the 500 °C sample is significantly reduced for the compound obtained at 1000 °C which contains large multidomain crystallites and less disorder (Figure 12c) leading also to a shift of the splitting of the zfc-fc curves to lower temperatures.

## Conclusions

We demonstrated that solution combustion is a powerful method to prepare a starting material for high-entropy spinels consisting of six transition metal cations. Due to the reductive atmosphere during the combustion reaction, metallic nanoparticles precipitated which was evidenced by PXRD and XANES

**Table 6.** Comparison of the saturation magnetization of the divalent ferrites in comparison to HES1s.

composition	$M_M$ Bulk [emu/g]	$M_M$ Nano (~ 15 nm) [emu/g]	Reference
MnFe <sub>2</sub> O <sub>4</sub>	98 (5 K)	54 (RT)	[47]
Fe <sub>3</sub> O <sub>4</sub>	92 (5 K)	56 (RT)	[48, 49]
CoFe <sub>2</sub> O <sub>4</sub>	94 (5 K)	30 (RT)	[50, 51]
NiFe <sub>2</sub> O <sub>4</sub>	53 (4.2 K)	23 (RT)	[48], [52]
CuFe <sub>2</sub> O <sub>4</sub>	33 (4.2 K)	27–51 (RT)	[53]
ZnFe <sub>2</sub> O <sub>4</sub>	0	65 (RT)	[54]
HEO 500 °C	–	71 (RT)	actual work
HEO 1000 °C	108 (5 K)	–	actual work

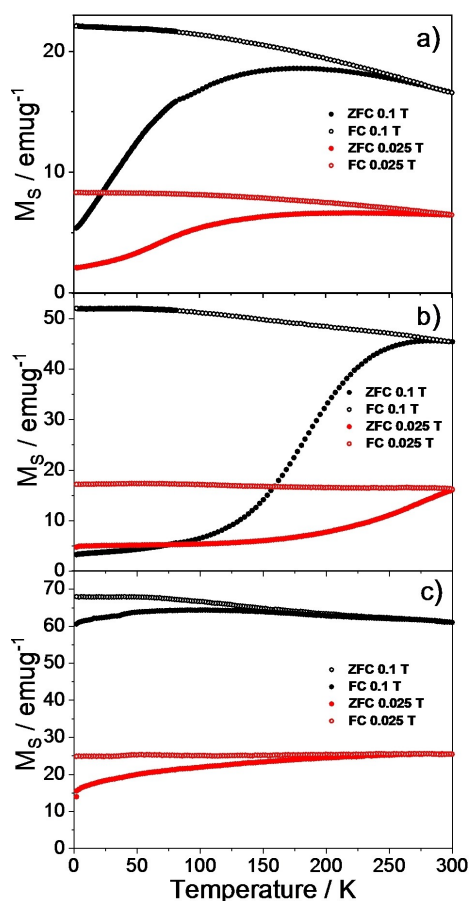


**Figure 12.** ZFC-FC curves of a) HES1 a.s., b) HES1 500 °C and c) HES1 1000 °C with an applied magnetic field of 1000 Oe and 250 Oe.

investigations. These nanoparticles, however, were completely integrated into the spinel structure by moderate thermal treatment without changing the sizes of coherently scattering domains in the nano-regime. Only at the highest temperature (1000 °C), a well crystalline sample was formed. Thus, we were able to synthesize and study a new class of high-entropy spinels, both as nanoscopic and as highly crystalline materials to get a deeper insight into the nature of such materials. The entropic stabilization of the spinel with general composition  $(A_{1,0.2}A_{2,0.2}A_{3,0.2}A_{4,0.2}A_{5,0.2})Fe_2O_4$  (A1-A5 represent transition metal cations) was evidenced by in situ PXRD and by removal of single constituents of the spinel. The excellent microscopic homogeneity is demonstrated by the PXRD data, SAED and HRTEM micrographs as well as STEM elemental mapping (for the 1000 °C sample). The results of Mössbauer measurements and the information extracted from XANES spectra indicate that  $\approx 2/3$  of the  $Fe^{3+}$  occupies the octahedral sites and  $\approx 1/3$  occupies the tetrahedral sites in the spinel structure, resulting in a degree of inversion of about 66%. The XANES data collected on the K-edges of the other elements suggest that a majority of the cations are randomly distributed between the octahedral and tetrahedral sites, except for  $Zn^{2+}$  which is solely in a tetrahedral coordination geometry and  $Cu^{2+}$  and eventually  $Ni^{2+}$  in an octahedral coordination. Ignoring the measurement

uncertainties and assuming full occupancy of the oxygen positions, the following spinel results from these data:  $(Co_{0.07}Mn_{0.1}Zn_{0.2}Fe_{0.67})_T(Co_{0.13}Ni_{0.2}Cu_{0.2}Mn_{0.1}Fe_{1.33})_O_4$ .

Magnetic studies show a remarkable high saturation magnetization, where the non-magnetic zinc on the tetrahedral sites is beneficial by inducing an imbalance of the magnetic moments in this antiferromagnetic system. In the present sample the random distribution of the magnetic cations over the crystallographic sites has a positive impact. While TEM and PXRD studies of the 500 °C sample indicate a single phase, the magnetic data show that there may be two magnetic components contributing to the hysteresis, raising the question of whether the magnetic studies are more sensitive and therefore reveal more subtleties of the microstructure. Spinels exhibit a number of outstanding physical properties that have long made them the target of numerous research efforts for a wide range of applications, such as energy storage or catalytic applications.<sup>[57–59]</sup> Therefore, research into this new class of spinels is an ideal prerequisite for the development of new innovative materials.

## Experimental

### Chemicals

Metal nitrates and glucose were purchased from Merck and Grüssing. All chemicals used in this study were used as received without further purification.

### Synthesis of $Cu_{0.2}Co_{0.2}Mn_{0.2}Ni_{0.2}Zn_{0.2}Fe_2O_4$ (HES1s)

0.47 g (1.6 mmol)  $Co(NO_3)_2 \cdot 6H_2O$ , 0.39 g (1.6 mmol)  $Cu(NO_3)_2 \cdot 3H_2O$ , 0.40 g (1.6 mmol)  $Mn(NO_3)_2 \cdot 4H_2O$ , 0.47 g (1.6 mmol)  $Ni(NO_3)_2 \cdot 6H_2O$ , 0.48 g (1.6 mmol)  $Zn(NO_3)_2 \cdot 6H_2O$ , 6.45 g (16.0 mmol)  $Fe(NO_3)_3 \cdot 9H_2O$  and 1.6 g (8.0 mmol) glucose were placed in a mortar and 2 drops of water were added until a homogenous viscous material was formed. The sample was transferred to a pre-heated ( $T=400$  °C, 30 min) round bottom flask with a heating coat and maintained at this temperature for 20 min. During the synthesis, gases evolved which were passed into a washing flask. The formed black powder was naturally cooled to room temperature through a drying column. Afterwards, the samples were subsequently sintered at different temperatures. Accordingly, the samples are labeled as HES1s a.s. (as synthesized) and HES1s T ( $T=500, 650$  and  $1000$  °C).

### Materials characterization

Powder X-ray diffraction (PXRD) investigations were carried out in transmission and reflexion geometry on a Panalytical Empyrean with  $Cu_{K\alpha}$  radiation ( $\lambda=1.54058$  Å), a focusing mirror and a PIXcel1D detector. Rietveld refinements<sup>[60]</sup> against the powder patterns were performed with the program Topas Academic 6.0.<sup>[61]</sup>

For the in situ temperature resolved XRPD experiments, an X'Pert Pro MPD diffractometer from PANalytical ( $Ni$ -filtered  $Cu_{K\alpha}$  radiation) with a PIXcel detector equipped with an Anton Paar HTK 1200 N high temperature chamber was used. The detector settings were adjusted to reduce the effect of sample fluorescence. Heating steps of 100 °C were applied in the temperature range 100–500 °C, above this range the increment was 25 °C until a temperature of 900 °C

was reached. All patterns were measured for ~20 min at constant temperature covering a  $2\theta$  range of 22–45°.

Total scattering X-ray experiments were performed in Debye–Scherrer geometry using high-energy synchrotron radiation (60 keV,  $\lambda=0.20708$  Å) at beamline P02.1 at Petra III (DESY, Hamburg). The total scattering patterns, collected with a XRD1621 Perkin Elmer amorphous silicon image plate detector at a distance of 354 mm, were transformed into atomic pair distribution functions (PDF),  $G(r)$ , using xPDFsuite.<sup>[62]</sup> An empty capillary was measured under identical conditions in order to subtract glass contributions to the PDF of the sample.  $\text{LaB}_6$  (NIST 660b) was used as standard material to calibrate the instrumental contribution. Theoretical models were fit to the PDF data in the range of 1.7 to 50.0 Å with PDFgui (details in the Supporting Information).<sup>[63]</sup>

SEM images and EDX data were recorded with a Gemini Ultra55Plus from Zeiss with a SD-Detector from Oxford. Acceleration voltage of 20 kV was applied to detect the K-lines of the elements.

Transmission electron microscopy (TEM): The crystallite size and the morphology were investigated by dark-field and bright-field TEM imaging, while the crystal structure analysis was performed by high-resolution TEM (HRTEM) and selected area electron diffraction (SAED) using a FEI Tecnai F30 STwin G<sup>2</sup> microscope with 300 kV acceleration voltage. For the chemical analysis scanning TEM (STEM), a high-angle annular dark-field detector, and energy dispersive X-ray spectroscopy (Si(Li) detector with EDAX system) was used. The TEM samples were prepared on Al grids with a thin carbon carrier film, therefore the sample powder was dispersed in butanol and drop-casted on the grid.

Analyses of the magnetic properties were done with a Quantum Design PPMS Model 600 in the ACMS setup applying magnetic fields between 1 and 9 Tesla at temperatures of 2–300 K. The samples were prepared from finely ground powder that was encapsulated into a gelatine capsule. The magnetization of the as synthesized sample (a.s.) sample was corrected for the amount of spinel obtained from the Rietveld refinement. A diamagnetic correction was not applied because the standard deviation of the measuring instrument is higher than the diamagnetic value of the samples.

<sup>57</sup>Fe Mössbauer spectroscopy was performed at room temperature in transmission mode with a constant acceleration spectrometer and a <sup>57</sup>Co(Rh) source. All isomer shifts are given relative to that of  $\alpha$ -Fe at room temperature.

X-Ray absorption spectroscopy: All samples were measured synchronously in fluorescence and transmission mode at the XAS beamline at the synchrotron at the KIT. Measurements were done with a Si<111>-crystal pair of the double crystal fixed exit monochromator (DCM). Oxford X-Spec ionizations chambers (filling adjusted to 15% in the first chamber, 30% in the second chamber, 60% signal absorption in the third chamber, calculated at 7.5 keV) were used as transmission detectors and an one-element Vortex<sup>®</sup>-90EX Silicon Drift Detector with XIA xMap detector-electronic for the fluorescence detection. Depending on the resulting signal-to-noise ratio either the transmission or the fluorescence signal was used for the XANES and EXAFS data evaluation. The measurements were undertaken inside a vacuum chamber to maximize the signal-to-noise ratio and reduce the possibility of beam-based sample damage. The samples were transferred with a sample transfer system. Data acquisition was done in step-by-step mode using constant steps of 5, 2 before and 0.5 eV before and in the edge region. After the edge region passed through, constant k-increments of 0.05 were used until the next absorption edge (12–13 k, Mn, Fe, Co, Ni) or until 16 k. Except for Zn K-edge scans the length of the spectra were limited by the start of the next absorption

edge. The  $k$ -range and thus the spatial resolution of EXAFS measurements were not limited by the noise but due to the limited  $k$ -range (especially Mn and Fe). These multiple absorption edges lead to a complex background, which is why software based on EXAFS123 in IgorPro (wavemetrics) was used for data analysis. (<https://web.archive.org/web/20051031210215/http://www.harverford.edu/chem/Scarrow/EXAFS123/>). The core functions of EXAFS123 allow one to analyze the data more accurately than many other EXAFS data analysis programs. In addition to the XANES and EXAFS background subtraction, PCA component analyses were applied based on the existing functions implemented in IgorPro. The XANES and EXAFS curves were extracted for all spectra and were added up as  $\mu$ d data.

## Supporting Information Summary

Supporting Information contains graphics of PDF analysis and crystallite morphology, SEM and TEM images and histograms of the crystallite sizes.

## Acknowledgments

Financial support by the State of Schleswig-Holstein is acknowledged. The authors thank the German Electron Synchrotron (DESY) and Huayna Terraschke for beamtime allocation. Furthermore, we would like to thank Dr.-Ing. Torben Dankwort for TEM investigations.

## Conflict of Interest

The authors declare no conflict of interest.

## Data Availability Statement

The data that support the findings of this study are available from the corresponding author upon reasonable request.

**Keywords:** High-entropy spinel oxides · Magnetic properties · Microstructure · Mössbauer spectroscopy · XANES

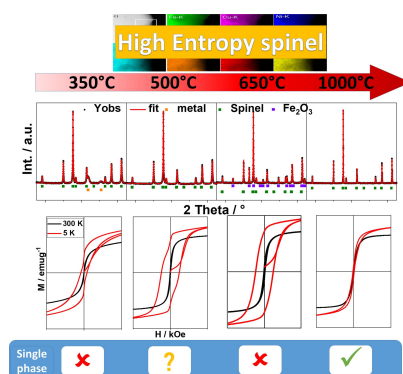
- [1] Y. Zhang, T. T. Zuo, Z. Tang, M. C. Gao, K. A. Dahmen, P. K. Liaw, Z. P. Lu, *Prog. Mater. Sci.* **2014**, *61*, 1.
- [2] S. Wei, F. He, C. C. Tasan, *J. Mater. Res.* **2018**, *33*, 2924.
- [3] J.-W. Yeh, *JOM* **2013**, *65*, 1759.
- [4] D. B. Miracle, J. D. Miller, O. N. Senkov, C. Woodward, M. D. Uchic, J. Tiley, *Entropy* **2014**, *16*, 494.
- [5] C. M. Rost, E. Sachet, T. Borman, A. Moballeghe, E. C. Dickey, D. Hou, J. L. Jones, S. Curtarolo, J.-P. Maria, *Nat. Commun.* **2015**, *6*, 8485.
- [6] R. Witte, A. Sarkar, R. Kruk, B. Eggert, R. A. Brand, H. Wende, H. Hahn, *Phys. Rev. Mater.* **2019**, *3*, 034406.
- [7] A. Mao, F. Quan, H.-Z. Xiang, Z.-G. Zhang, K. Kuramoto, A.-L. Xia, *J. Mol. Struct.* **2019**, *1194*, 11.
- [8] J. Dąbrowa, M. Stygar, A. Mikula, A. Knapik, K. Mroczka, W. Tejchman, M. Danielewski, M. Martin, *Mater. Lett.* **2018**, *216*, 32.
- [9] A. Mao, H.-Z. Xiang, Z.-G. Zhang, K. Kuramoto, H. Zhang, Y. Jia, *J. Magn. Mater.* **2020**, *497*, 165884.

- [10] Z. Grzesik, G. Smoła, M. Miszczak, M. Stygar, J. Dąbrowa, M. Zajusz, K. Świerczek, M. Danielewski, *J. Eur. Ceram. Soc.* **2020**, *40*, 835.
- [11] M. Stygar, J. Dąbrowa, M. Moździerz, M. Zajusz, W. Skubida, K. Mroczka, K. Berent, K. Świerczek, M. Danielewski, *J. Eur. Ceram. Soc.* **2020**, *40*, 1644.
- [12] M. Fracchia, M. Manzoli, U. Anselmi-Tamburini, P. Ghigna, *Scr. Mater.* **2020**, *188*, 26.
- [13] D. Wang, Z. Liu, S. Du, Y. Zhang, H. Li, Z. Xiao, W. Chen, R. Chen, Y. Wang, Y.-G. Liu, S. Wang, *J. Mater. Chem. A* **2019**, *7*, 24211.
- [14] H. Chen, N. Qiu, B. Wu, Z. Yang, S. Sun, Y. Wang, *RSC Adv.* **2020**, *10*, 9736.
- [15] K.-H. Tian, C.-Q. Duan, Q. Ma, X.-L. Li, Z.-Y. Wang, H.-Y. Sun, S.-H. Luo, D. Wang, Y.-G. Liu, *Rare Met.* **2022**, *41*, 1265.
- [16] Z. Sun, Y. Zhao, C. Sun, Q. Ni, C. Wang, H. Jin, *Chem. Eng. J.* **2022**, *431*, 133448.
- [17] B. Wang, J. Yao, J. Wang, A. Chang, *J. Alloys Compd.* **2022**, *897*, 163188.
- [18] K. Chen, X. Pei, L. Tang, H. Cheng, Z. Li, C. Li, X. Zhang, L. An, *J. Eur. Ceram. Soc.* **2018**, *38*, 4161.
- [19] S. Jiang, T. Hu, J. Gild, N. Zhou, J. Nie, M. Qin, T. Harrington, K. Vecchio, J. Luo, *Scr. Mater.* **2018**, *142*, 116.
- [20] G. Wang, J. Qin, Y. Feng, B. Feng, S. Yang, Z. Wang, Y. Zhao, J. Wei, *ACS Appl. Mater. Interfaces* **2020**, *12*, 45155.
- [21] S. K. Shaw, A. Gangwar, A. Sharma, S. K. Alla, S. Kavita, M. Vasundhara, S. S. Meena, P. Maiti, N. K. Prasad, *J. Alloys Compd.* **2021**, *878*, 160269.
- [22] F. Marik, D. Singh, B. Gonano, F. Veillon, D. Pelloquin, Y. Bréard, *Scr. Mater.* **2020**, *186*, 366.
- [23] S. Marik, D. Singh, B. Gonano, F. Veillon, D. Pelloquin, Y. Bréard, *Scr. Mater.* **2020**, *183*, 107.
- [24] F. Hosseini Mohammadabadi, S. M. Masoudpanah, S. Alamolhoda, H. R. Koohdar, *J. Alloys Compd.* **2022**, *909*, 164637.
- [25] B. Musić, Q. Wright, T. Z. Ward, A. Grutter, E. Arenholz, D. Gilbert, D. Mandrus, V. Keppens, *Phys. Rev. Mater.* **2019**, *3*, 104416.
- [26] A. Sarkar, R. Kruk, H. Hahn, *Dalton Trans.* **2021**, *50*, 1973.
- [27] J. Cieslak, M. Reissner, K. Berent, J. Dąbrowa, M. Stygar, M. Moździerz, M. Zajusz, *Acta Mater.* **2021**, *206*, 116600.
- [28] A. Sarkar, B. Eggert, R. Witte, J. Lill, L. Velasco, Q. Wang, J. Sonar, K. Ollefs, S. S. Bhattacharya, R. A. Brand, H. Wende, F. M. F. de Groot, O. Clemens, H. Hahn, R. Kruk, *Acta Mater.* **2022**, *226*, 117581.
- [29] J. Z. Msomi, T. Moyo, J. J. Dolo, *Hyperfine Interact.* **2010**, *197*, 59.
- [30] M. Stoia, C. Păcurariu, E.-C. Muntean, *J. Therm. Anal. Calorim.* **2017**, *127*, 155.
- [31] E. Ranjith Kumar, T. Arunkumar, T. Prakash, *Superlattices Microstruct.* **2015**, *85*, 530.
- [32] K. Heinemann, H. Poppa, *Surf. Sci.* **1985**, *156*, 265.
- [33] S. Bid, S. K. Pradhan, *Mater. Chem. Phys.* **2003**, *82*, 27.
- [34] Z. Tian, C. Zhu, J. Wang, Z. Xia, Y. Liu, S. Yuan, *J. Magn. Magn. Mater.* **2015**, *377*, 176.
- [35] S. Permien, S. Indris, M. Scheuermann, U. Schürmann, V. Mereacre, A. K. Powell, L. Kienle, W. Bensch, *J. Mater. Chem. A* **2015**, *3*, 1549.
- [36] S. Permien, H. Hain, M. Scheuermann, S. Mangold, V. Mereacre, A. K. Powell, S. Indris, U. Schürmann, L. Kienle, V. Duppel, S. Harm, W. Bensch, *RSC Adv.* **2013**, *3*, 23001.
- [37] S. J. Oh, D. C. Cook, H. E. Townsend, *Hyperfine Interact.* **1998**, *112*, 59.
- [38] V. Šepelák, A. Feldhoff, P. Heitjans, F. Krumeich, D. Menzel, F. J. Litterst, I. Bergmann, K. D. Becker, *Chem. Mater.* **2006**, *18*, 3057.
- [39] V. Šepelák, I. Bergmann, A. Feldhoff, P. Heitjans, F. Krumeich, D. Menzel, F. J. Litterst, S. J. Campbell, K. D. Becker, *J. Phys. Chem. C* **2007**, *111*, 5026.
- [40] R. Topkaya, Ö. Akman, S. Kazan, B. Aktaş, Z. Durmus, A. Baykal, *J. Nanopart. Res.* **2012**, *14*, 1156.
- [41] Ö. Iglesias, A. Labarta, *Phys. Condens. Matter* **2004**, *343*, 286.
- [42] M. Rahimi, P. Kameli, M. Ranjibar, H. Salamati, *J. Nanopart. Res.* **2013**, *15*, 1865.
- [43] Y. Kumar, P. M. Shirage, *J. Mater. Sci.* **2017**, *52*, 4840.
- [44] Q. Song, Z. J. Zhang, *J. Phys. Chem. B* **2006**, *110*, 11205.
- [45] Ö. Özdemir, D. J. Dunlop, T. S. Berquó, *Geochem. Geophys. Geosyst.* **2008**, *9*.
- [46] A. B. Gadkari, T. J. Shinde, P. N. Vasambekar, *J. Mater. Sci. Mater. Electron.* **2009**, *21*, 96.
- [47] B. Aslibeiki, P. Kameli, M. H. Ehsani, *Ceram. Int.* **2016**, *42*, 12789.
- [48] A. Berkowitz, J. Lahut, C. VanBuren, *IEEE Trans. Magn.* **1980**, *16*, 184.
- [49] Y. Wei, B. Han, X. Hu, Y. Lin, X. Wang, X. Deng, *Procedia Eng.* **2012**, *27*, 632.
- [50] Z. Chen, L. Gao, *Mater. Sci. Eng. B* **2007**, *141*, 82.
- [51] J. L. López, H.-D. Pfannes, R. Paniago, J. P. Sinnecker, M. A. Novak, *J. Magn. Magn. Mater.* **2008**, *320*, e327.
- [52] M. Salavati-Niasari, F. Davar, T. Mahmoudi, *Polyhedron* **2009**, *28*, 1455.
- [53] G. F. Goya, H. R. Rechenberg, J. Z. Jiang, *J. Appl. Phys.* **1998**, *84*, 1101.
- [54] Z. Ž. Lazarević, Č. Jovalekić, V. N. Ivanovski, A. Rečnik, A. Milutinović, B. Cekić, N. Ž. Romčević, *J. Phys. Chem. Solids* **2014**, *75*, 869.
- [55] M. George, S. S. Nair, A. M. John, P. A. Joy, M. R. Anantharaman, *J. Phys. Appl. Phys.* **2006**, *39*, 900.
- [56] H. Yang, Z. Wang, L. Song, M. Zhao, J. Wang, H. Luo, *J. Phys. Appl. Phys.* **1996**, *29*, 2574.
- [57] T. Tatarchuk, M. Bououdina, J. Judith Vijaya, L. John Kennedy, in *Nanophysics Nanomater. Interface Stud. Appl.* (Eds: O. Fesenko, L. Yatsenko), Springer International Publishing, Cham **2017**, 305.
- [58] K. K. Kefeni, B. B. Mamba, *Sustain. Mater. Technol.* **2020**, *23*, e00140.
- [59] O. Vozniuk, N. Tanchoux, J.-M. Millet, S. Albonetti, F. Di Renzo, F. Cavani, in *Stud. Surf. Sci. Catal.* (Eds: S. Albonetti, S. Perathoner, E. A. Quadrelli), Elsevier **2019**, 281.
- [60] H. M. Rietveld, *J. Appl. Crystallogr.* **1969**, *2*, 65.
- [61] A. A. Coelho, **2016**, TOPAS Academic, Version 6, *Coelho Software*, Brisbane.
- [62] X. Yang, P. Juhas, C. L. Farrow, S. J. L. Billinge, **2015**, arXiv Preprint arXiv:1402.3163 [Cond-Mat]. DOI: <https://doi.org/10.48550/arXiv.1402.3163>.
- [63] C. L. Farrow, P. Juhas, J. W. Liu, D. Bryndin, E. S. Božin, J. Bloch, T. Proffen, S. J. L. Billinge, *J. Phys. Condens. Matter* **2007**, *19*, 335219.

Manuscript received: July 5, 2022

## RESEARCH ARTICLE

A high entropy spinel with the formula  $A_{1,0,2}A_{2,0,2}A_{3,0,2}A_{4,0,2}A_{5,0,2}Fe_2O_4$  was synthesized via a solution combustion method and treated at different annealing temperatures. During all the steps the product was investigated via a multi-method approach with some astonishing results regarding the truth of its single-phase nature.



S. Senkale, Dr. M. Kamp, Dr. S. Mangold, Dr. S. Indris, Prof. Dr. L. Kienle, Dr. R. K. Kremer, Prof. Dr. W. Bensch\*

1 – 17

**Multi-Method Characterization of the High-Entropy Spinel Oxide  $Mn_{0,2}Co_{0,2}Ni_{0,2}Cu_{0,2}Zn_{0,2}Fe_2O_4$ : Entropy Evidence, Microstructure, and Magnetic Properties**